Nfe2l1-mediated proteasome function controls muscle energy metabolism in obesity

Imke L. Lemmer[1,2], Daniel T. Haas[3], Nienke Willemsen[1], Stefan Kotschi[1], Irmak Toksöz[1], Ejona Gjika[1], Sajjad Khani[1], Maria Rohm[2,7], Nick Diercksen[4,5], Phong B.H. Nguyen[4,6,7], Michael P. Menden[4,6,7], Desalegn T. Egu[8], Jens Waschke[8], Steen Larsen[9,10], Tao Ma[11], Zachary Gerhart-Hines[11], Stephan Herzig[2,7,12-14], Kenneth Dyar[2,7], Natalie Krahmer[3] & Alexander Bartelt[1,2,7,12,15*]

[1]Institute for Cardiovascular Prevention (IPEK), Ludwig-Maximilians-University Munich, Munich, Germany
[2]Institute for Diabetes and Cancer (IDC), Helmholtz Center Munich, German Research Center for Environmental Health, Neuherberg, Germany
[3]Institute for Diabetes and Obesity (IDO), Helmholtz Center Munich, German Research Center for Environmental Health, Neuherberg, Germany
[4]Institute of Computational Biology, Helmholtz Center Munich, 85764 Neuherberg, Germany
[5]Department of Bioengineering Sciences, Weihenstephan-Triesdorf University of Applied Sciences
[6]Department of Biology, Ludwig-Maximilians-University Munich, 82152 Martinsried, German
[7]German Center for Diabetes Research (DZD), 85764 Neuherberg, Germany
[8]Chair of Vegetative Anatomy, Institute of Anatomy, Faculty of Medicine, Ludwig-Maximilians-University Munich, Munich, Germany
[9]Xlab, Center for Healthy Aging, Department of Biomedical Sciences, University of Copenhagen, Copenhagen, Denmark
[10]Clinical Research Centre, Medical University of Bialystok, Bialystok, Poland
[11]Novo Nordisk Foundation Center for Basic Metabolic Research, University of Copenhagen, Copenhagen, Denmark
[12]German Center for Cardiovascular Research, Partner Site Munich Heart Alliance, LMU Hospital, Munich, Germany
[13]Joint Heidelberg-IDC Translational Diabetes Unit, Inner Medicine I, Heidelberg University Hospital, Germany
[14]Chair Molecular Metabolic Control, Technical University Munich, Germany
[15]Department of Molecular Metabolism & Sabri Ülker Center for Metabolic Research, Harvard T.H. Chan School of Public Health, Boston, USA

*Correspondence: Alexander Bartelt, alexander.bartelt@med.uni-muenchen.de

Keywords: Obesity, skeletal muscle, proteostasis, UPS, Nfe2l1

Abstract

Muscle function is an important denominator of energy balance and metabolic health. Adapting the proteome to energetic challenges, in response to diet or fasting, is facilitated by programs of proteostasis, but the adaptive role of the ubiquitin-proteasome system (UPS) in muscle remains unclear. Here, using a multi-omics approach, we uncover that the distinct metabolic condition of obesity is associated with recalibration of the UPS in muscle. Interestingly, obesity is associated with the activation of the transcription factor Nuclear factor erythroid 2-like 1 (Nfe2l1, also known as Nrf1), and loss of myocyte Nfe2l1 diminishes proteasomal activity and leads to hyperubiquitylation. Mice lacking Nfe2l1 display hormetic energy metabolism and resistance to diet-induced obesity, associated with a lean phenotype and muscle fiber type switching. In conclusion, we define a new adaptive role for UPS in remolding of muscle proteome and function, which is controlled by fine-tuning of proteasome function by Nfe2l1.

Introduction

Obesity is an extreme metabolic condition, in which chronic overnutrition leads to excessive weight gain and deterioration of cellular quality control mechanisms[1–3].The endoplasmic reticulum (ER) is a central hub where protein, lipid, and parts of glucose metabolism are sensed and regulated in an adaptive manner to avoid cellular stress and inflammation[4–6]. These stress resistance mechanisms include activation of the integrated stress response, and a large body of evidence implicates the unfolded protein response (UPR) and autophagy as evolutionary conserved quality control mechanisms involved in this process. However, much less is known about the role of the ubiquitin-proteasome system (UPS), and specifically ER-associated protein degradation (ERAD) as an alternative pathway by which cells mitigate proteotoxicity and maintain proteostasis.

In this context, we and others have shown that UPS activity, rather than being static, is fine-tuned through multiple regulatory mechanisms[7]. An important transcriptional component of matching proteasomal activity to cellular demands is Nuclear factor erythroid 2-like 1 (Nfe2l1, also known as Nrf1 or TCF11), which belongs to the bZIP cap'N'collar family of transcription factors[8]. If proteasomal activity is compromised, e.g. in the presence of chemical proteasome inhibitors, Nfe2l1 increases the expression of proteasomal subunits, thereby adapting proteasomal activity to proteostatic needs[9]. Nfe2l1 activity is subject to complex posttranslational regulation, as Nfe2l1 is tethered to the ER membrane, continuously undergoes translocation across the membrane, proteolytic cleavage, and deglycosylation before the remaining fragment becomes transcriptionally active. During cellular homeostasis, the DNA-binding Nfe2l1 fragment itself is ubiquitylated and degraded and, thus virtually absent in cells. When proteasome function is suboptimal, Nfe2l1 escapes degradation and restores proteasomal activity. While most of this mechanistic insight was defined in the context of cancer cells, recent studies have shed light on the physiological role of Nfe2l1-mediated proteasome function[10,11]. Nfe2l1 is activated by cold exposure in thermogenic adipocytes, and its proteasomal stimulation is a critical factor for fine-tuning UPS activity. Compromised proteasome function, by either chemical inhibition or loss of Nfe2l1, is associated with ER stress and diminished non-shivering thermogenesis mediated by brown fat[10]. The adaptive nature of Nfe2l1 raises the question whether fine-tuning of proteostasis is a quality control mechanism in other physiologic or pathological conditions in metabolically relevant organs beyond brown fat.

Skeletal muscle has major roles in metabolism, and muscle activity is associated with maintenance of metabolic homeostasis[12]. For example, skeletal muscle acts as a sink for glucose, is a store of amino acids, and markedly contributes to whole-body energy expenditure[13]. Conversely, obesity is associated with compromised muscle function, fatigue, inflammation, and insulin resistance[13]. While the role of some proteostatic mechanisms such as UPR and autophagy for muscle atrophy is well established[14–19], the relevance of Nfe2l1-mediated fine-tuning of UPS for muscle biology, and specifically in obesity are unknown. Here, we investigate remodeling of the muscle UPS in obesity and define the role of Nfe2l1 as a new regulator of muscle biology.

Results

Rewiring of skeletal muscle UPS in obesity is linked to Nfe2l1.

Obesity is a challenging metabolic condition, but little is known about modulation of the UPS induced by associated alterations in hormonal, nutrient, or energetic homeostasis in muscle. We first asked whether muscle proteasomal activity, the driving force of protein degradation by the UPS, is regulated in obesity. Using fluorometric assays (Fig. 1A) as well as a native PAGE analysis (Fig. 1B) we found that proteasomal activity in gastrocnemius (GC) muscles, a mixed muscle tissue, predominantly consisting of fast-twitch fibers located in the hind limb, of high-fat diet (HFD)-induced obese mice (DIO) is markedly higher compared to chow fed, lean controls. This increase in activity was associated with higher levels of 20S proteasome subunits (Fig. 1C). To define the nature of this UPS remodeling and its impact on muscle protein composition, we took an unbiased approach via mass spectrometry (MS) to define the proteomic landscape of muscle in DIO mice. Specifically, we determined the content of ubiquitylated proteins and sites of ubiquitylation (ubiquitome) by immunoprecipitation of the Diglycine (DiGly)-remnant motif of ubiquitin (Fig. 1D). The challenge of skeletal muscle proteomics is the high amount of structural proteins, which limit the identification of proteins with lower abundance[20,21]. Nevertheless, we quantified 3739 proteins in the proteome and 1685 ubiquitylated peptides in the ubiquitome. While the volcano plots of the total proteome (Fig. 1E) and ubiquitome (Fig. 1F) showed significant changes upon HFD feeding the total levels of ubiquitylated proteins and poly-ubiquitylation sites remained unchanged (Fig. 1G). Next, we analyzed the global changes in the UPS. However, as higher abundance in the proteome can theoretically increase detection in the ubiquitome[22], we normalized ubiquitylated proteins to their respective protein amount and performed gene ontology (GO) analysis (Fig.1 H,I). This analysis displayed that in DIO animals, pathways linked to ERAD and UPS are upregulated (Fig. 1H), whereas pathways associated with the generation of precursor metabolites and energy as well as generation of energy from oxidation reactions are significantly downregulated (Fig. 1I). Interestingly, upon HFD feeding we detected higher expression levels of the transcription factor Nfe2l1 (Fig.1J). In human muscle, we noted that *NFE2L1* is highly expressed, at much higher levels compared to other established muscle regulators, such as *NFE2L2* or *PPARGC1A* (Fig. 1K)[23]. In addition, in mouse muscle tissues, *Nfe2l1* mRNA expression is markedly higher in skeletal muscle than in brown fat or the heart (Fig. 1L). In conclusion, these data point towards an adaptive remodeling of the UPS in skeletal muscle during obesity, and potentially suggest an important role for Nfe2l1 in this process.

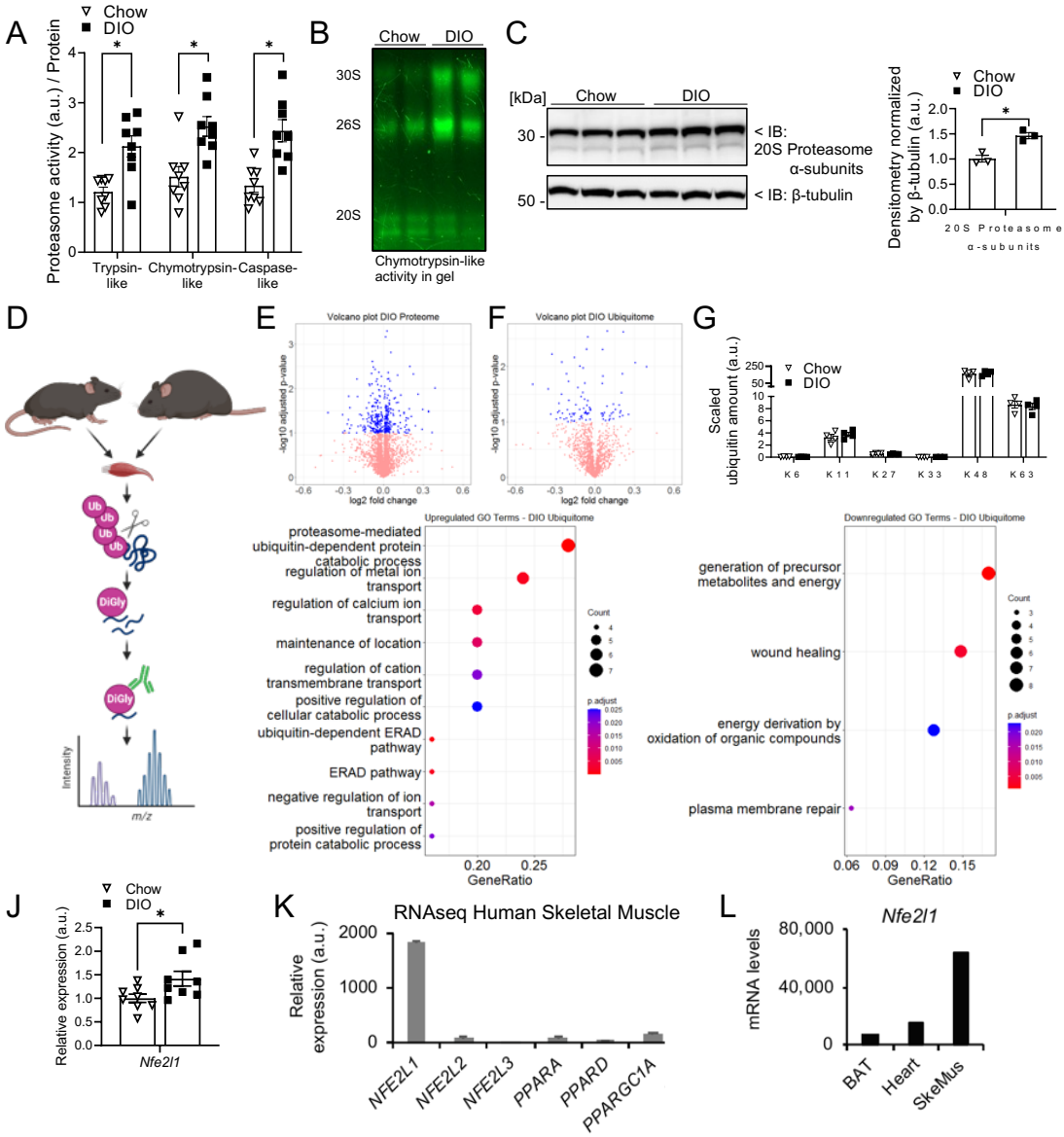

Figure 1: Obesity-induced remodeling of the ubiquitin-proteasome system (UPS) in skeletal muscle. (A-I) Assessment of UPS in gastrocnemius muscle (GC) of chow and diet-induced obesity mice after 16 weeks of high-fat diet (HFD): (A) Fluorometric assay of proteasome activity (n = 8 mice per group). (B) Representative In-gel chymotrypsin-like activity. (C) Immunoblot and quantification of protein levels of 20S Proteasome α-ring subunits. (D) Workflow of ubiquitome analysis via mass spectrometry (ubiquitomics). (E) Volcano plot of total proteome from chow controls and DIO mice. (F) Volcano plot of ubiquitome of DIO mice and lean controls. (G) Scaled amount of lysine (K)-linkages in ubiquitin. (H) Gene ontology (GO) pathway analysis of the top upregulated hits and (I) the most downregulated hits in the ubiquitome from DIO mice normalized to total proteome (n = 4 mice per group). (J) Relative expression levels of *Nfe2l1* in GC tissue of chow and DIO mice. (K) Relative expression of *NFE2L1* and related transcription factors in human skeletal muscle. (L) Absolute mRNA levels of *Nfe2l1* in different murine tissues. Data are mean ±SEM, $p<0.05$ by two-way analysis of variance (ANOVA) (A,D,G), *t*-test (C,J), $p<0.1$ and *t*-test (E-F), $p<0.2$ and *t*-test (H,I).

Loss of myocyte Nfe2l1 results in muscle remodeling and a lean phenotype.

Our finding that UPS and specifically proteasomal activity is a regulated process in obesity raises the question of potential mediators of this adaptive response. Recently, we have demonstrated that Nfe2l1 is a physiological transcriptional regulator of the UPS.[10] Nfe2l1 is known to be activated by proteasome inhibitors[8], but the impact of *Nfe2l1* on muscle biology is unknown. To determine the impact of Nfe2l1 loss *in vivo* we generated a transgenic Cre-

loxP mouse model with a skeletal myocyte-specific deletion of Nfe2l1 by using Acta1-Cre (*Nfe2l1* mKO). First, we noticed that mKO mice displayed a lower body weight, which was predominantly caused by lower lean mass, but not fat mass, compared to controls (Fig. 2A-C). Most prominently, gastrocnemius (GC) muscle was reduced in size and weight, which was associated with lower grip strength in *Nfe2l1* mKO mice compared to wild-type (WT) controls (Fig. 2D-F). Histological analyses by hematoxylin and eosin (H&E) staining, fiber typing, and succinate dehydrogenase, a complex of the electron transport chain, staining revealed major phenotypic change of GC (Fig. 2G), indicating a shift towards a more oxidative profile. In addition, analysis of myosin heavy chain expression by RNAseq supported the phenotypic switch towards more oxidative fibers, by an increase of slow-twitch *Myh7* and a decreased of fast-twitch *Myh2* expression (Fig. 2H). Furthermore, the perinatal myosin heavy chains *Mhy3* and *Mhy8* showed a significant upregulation in mKO mice, which suggests an ongoing regeneration of damaged fibers (Fig. 2H). To characterize the muscle ultrastructure, we performed transmission electron microscopy and we found that loss of Nfe2l1 leads to aberrant myofibrillar organization with mitochondrial alterations. The mitochondria of the mKO animals seem bulged and disrupted (Fig. 2I). Interestingly, muscle tissue from mKO mice contained less coenzyme Q: cytochrome-c-reductase, a component of OXPHOS complex-III (Fig. 2J). As it is acknowledged that structural alterations of mitochondria cristae impact respiration[24], we tested the functional consequences of this phenotype by performing Oroboros analysis, to determine mitochondrial oxygen consumption of GC muscle from *Nfe2l1* mKO and WT control mice. This experiment revealed less respiration after addition of ADP and succinate as well as reduced maximal respiration capacity in isolated muscle fibers of mKO mice compared to WT controls (Fig. 2K). To further pinpoint these results, we performed Seahorse analysis from isolated mitochondria, which confirmed the lower maximal respiration capacity in the mKO GC muscle mitochondria compared to WT controls (Fig. 2L). In summary, this set of data demonstrates a fiber type switch from fast to slow-twitch fiber with aberrant mitochondrial bioenergetics in mice lacking myocyte Nfe2l1.

Nfe2l1 regulates adaptive proteasome function in muscle and myocytes.

Thus far, our results indicate that Nfe2l1-mediated proteasome function is a critical component of myocyte proteostasis, metabolism and muscle tissue phenotype. To understand the relationship of Nfe2l1 and myocyte UPS, we used differentiated C2C12 cells and silenced *Nfe2l1* gene expression by siRNA. This strategy was successful, as both mRNA and protein Nfe2l1 levels were diminished, even after treatment with epoxomicin, a chemical proteasome inhibitor (Fig. 3A, B). Absence of Nfe2l1 led to lower levels of proteasome subunit gene expression (fig. 3A) and, consequently lower chymotrypsin-like proteasomal activity (Fig. 3C) along with higher levels of ubiquitylated proteins after proteasome inhibition with bortezomib compared to control cells treated with bortezomib (Fig. 3D). In summary, these results establish *Nfe2l1* as an adaptive regulator of proteasomal activity and ubiquitylation in cultured myocytes. To define the impact *in vivo*, we investigated the phenotype of *Nfe2l1* mKO mice. Similar to the *in vitro* model, genetic deletion of Nfe2l1 led to markedly lower proteasome subunit gene expression in muscle compared to WT control mice (Fig. 3E). Consequently, *ex vivo* proteasomal activity in muscle tissue of *Nfe2l1* mKO animals was blunted using both fluorometric assays as well as in the native PAGE (Fig. 3G,H), resulting in markedly higher levels of ubiquitylation (Fig. 3I). Interestingly, trypsin-like activity was higher in tissue from *Nfe2l1* mKO mice, indicating a possible dynamic remodeling of proteasomal activity independently of *Nfe2l1*. In conclusion, these data demonstrate the importance of myocyte Nfe2l1 *in vitro* and *in vivo* for UPS and for proteasome function in skeletal muscle.

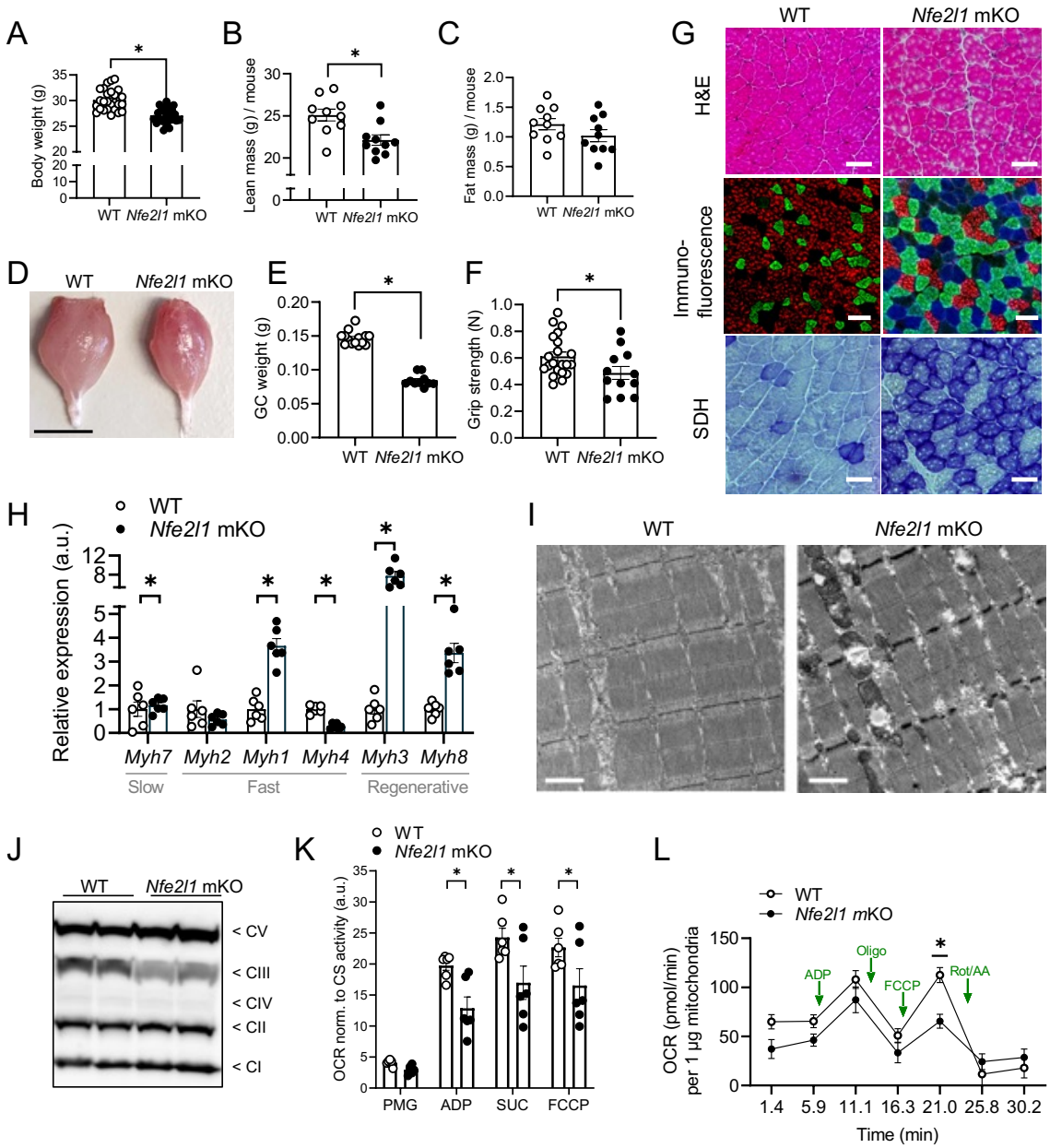

Figure 2: Loss of Nfe2l1 induces a muscle fiber type switch and a lean phenotype.
(A) Bodyweight of wild-type (WT) and mKO mice at 3 months (*n* = 26 - 27 mice per group). (B) Lean mass and (C) fat mass of *Nfe2l1* mKO mice and WT control (*n* = 10 mice per group). (D) Representative photograph of WT and *Nfe2l1* mKO gastrocnemius. Scale bar: 0.5 cm. (E) Weights of gastrocnemius (GC) of WT and mKO mice (*n* = 10-14 mice per group). (F) Forelimb grip strength of WT controls and mKO mice (*n* = 12 - 21 mice per group). (G) Representative hematoxylin and eosin (H&E)-stained, Immunofluorescent stained fiber types MyHC-2B (red), MyHC-2A (green), MyHC-1 (blue) and succinate dehydrogenase (SDH) stained complex II in the mitochondrial respiratory chain in GC of WT and mKO mice (scale bars: 50µm). (H) Relative expression levels of myosin heavy chains in GC tissue from *Nfe2l1* mKO mice and WT controls (*n* = 6 mice per group). (I) Representative transmission electron microscopy (TEM) images of WT and mKO GC, longitudinal sections. Scale bar: 1µm. (J) Immunoblot of complexes CI-CV of the electron transport chain. (K) OCR of GC fibers from WT and mKO animals normalized to citrate synthase (CS) activity (*n* = 6 mice per group). (L) Traces of oxygen consumption rate (OCR) from isolated mitochondria from WT and *Nfe2l1* mKO mice GC tissue (*n* = 4-6 mice per group). Data are mean ±SEM, $p<0.05$ by *t*-test (A-C, E-F, L) or 2-way ANOVA (H,K).

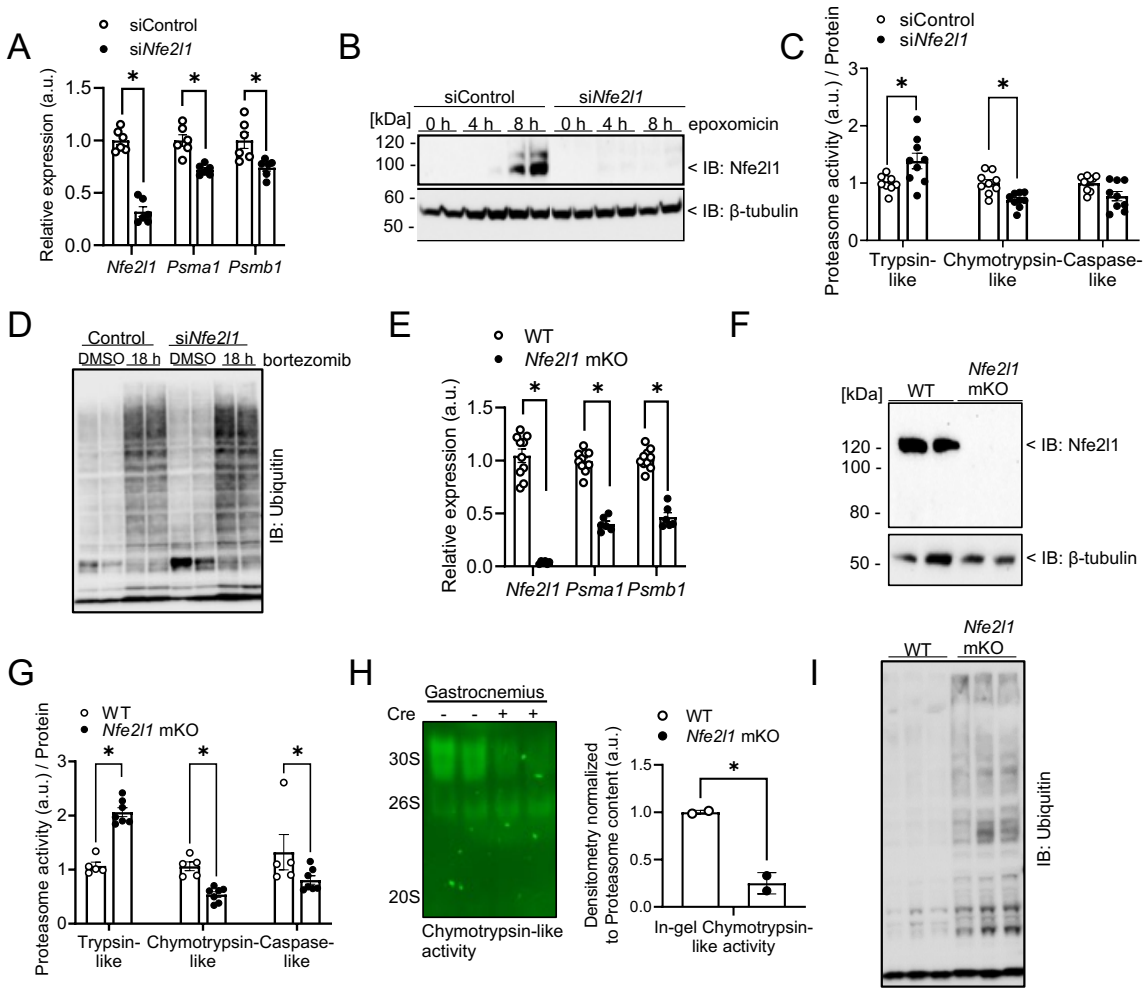

Figure 3: Loss of myocyte *Nfe2l1* results in hyperubiquitylation and reduced proteasome activity. (A-D) Protein and mRNA levels of *Nfe2l1* and downstream targets in C2C12 myocytes with siControl or si*Nfe2l1:* (A) Relative gene expression of *Nfe2l1* and proteasomal subunits *Psma1* and *Psmb1* (*n* = 3 technical replicates from 2 independent experiments). (B) Immunoblot of Nfe2l1 with epoxomicin treatment. (C) Fluorometric assay of proteasomal activity (*n* = 3 technical replicates from 3 independent experiments) and (D) Immunoblot of ubiquitylated proteins with bortezomib treatment. (E-I) Analysis of mRNA and protein levels in GC muscle tissue from WT controls and *Nfe2l1* skeletal muscle (Acta1-Cre) knock-out (mKO) mice: (E) Relative gene expression of *Nfe2l1* and proteasomal subunits *Psma1* and *Psmb1* (*n* = 6 -10 mice per group). (F) Representative Immunoblot of Nfe2l1. (G) Fluorometric assay of proteasomal activity (*n* = 5 - 7 mice per group). (H) Representative Nu-PAGE analysis of chymotrypsin-like proteasomal activity with densitometry analysis. (I) Immunoblot of ubiquitylated proteins. Data are mean ±SEM, p<0.05 by *t*-test (H) or 2 way ANOVA (A,C,E,G).

Loss of myocyte Nfe2l1 results in proteomic hyperubiquitylation.

The observation that loss of *Nfe2l1* leads to increased levels of ubiquitin prompted us to investigate the ubiquitome of muscle from *Nfe2l1* mKO mice and controls by MS as described above. The impact of *Nfe2l1* mKO on the proteome was marked with 2832 hits in total (Fig. 4A). Moreover, the ubiquitome was profoundly altered, as seen in the principal component analysis as well as in the volcano plot (Fig. 4B, C). The proteome showed many significantly regulated hits and in general a higher protein load in the mKO condition (Fig. 4A), potentially caused by impaired proteasomal protein degradation. GO analysis of the proteome highlighted energy metabolism and filament organization as major pathways affected in muscle from mKO mice compared to control tissue (Fig. 4D). KEGG pathway analysis revealed drastically lower levels of proteasome subunits in the proteome (Fig. 4E). In the ubiquitome, we found pathways

relevant to muscle structural organization and function as well as related to the UPS (Fig. 4F). Moreover, as not all posttranslational modifications with ubiquitin lead to degradation by the proteasome, we sought to determine the lysine (K)-linkages of the polyubiquitin chains. The data supported the hypothesis that Nfe2l1 stimulates protein degradation via the proteasome, as the dominant lysine-linkage was the proteasome-targeting linkage K48, accounting for more than 86% and being significantly higher in muscle of mKO mice compared to tissue of WT controls (Fig. 4G). To conclude, this unbiased global data set underscores the critical role of Nfe2l1 for UPS and proteostasis in skeletal muscle, pointing towards important roles of this process for muscle function and energy metabolism.

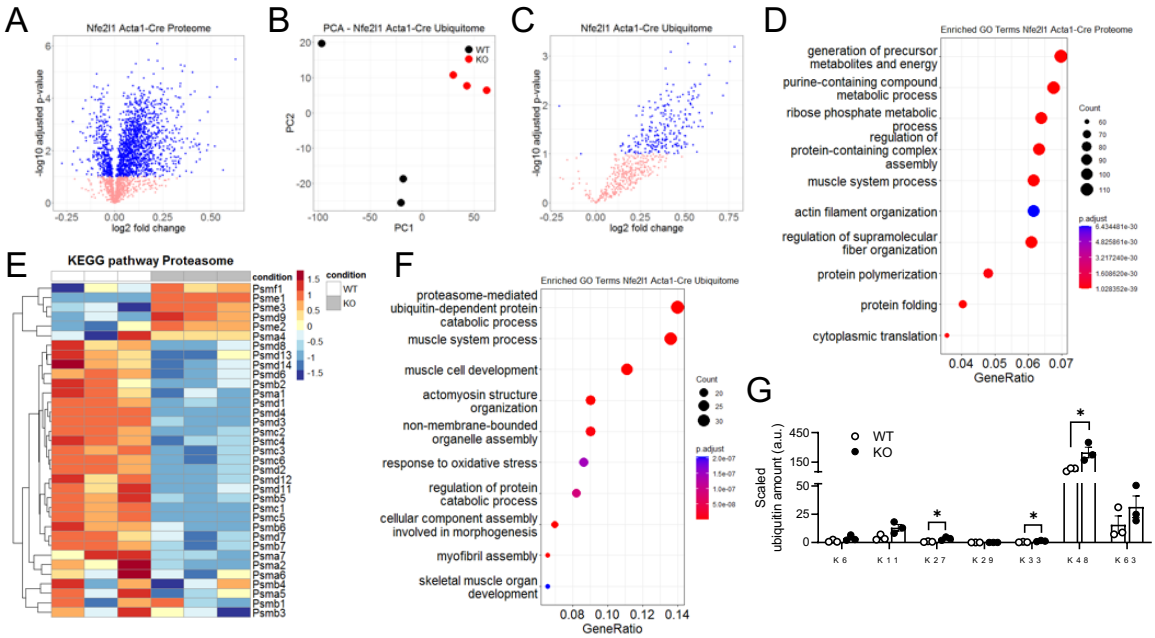

Figure 4: Myocyte Nfe2l1 shapes the ubiquitin landscape in skeletal muscle.
(A-G) Assessment of GC tissue from *Nfe2l1* mKO mice and WT controls via mass spectrometry (n = 3 mice per group): (A) Volcano plot of total proteome (B) PCA of genotypes in the ubiquitome. (C) Volcano plot of ubiquitome. (D) GO analysis and (E) KEGG-pathway analysis of proteasome (mmu03050) in the total proteome. (F) GO term enrichment analysis in the ubiquitome. (G) Relative amount of ubiquitin lysine (K)-linkages. Data are mean ±SEM, $p<0.1$ by t-test (A-F) or $p<0.05$ 2-way ANOVA (G).

Nfe2l1 shapes UPS predominantly in fast-twitch muscle fibers.

We wanted to understand how loss of Nfe2l1 translates to the muscle phenotype in the different fiber types and determine specific effects on the individual tissues. Therefore, we performed RNAseq analysis of soleus and GC as well as metabolomics of GC from *Nfe2l1* mKO mice. Volcano plot of the soleus shows a minimal impact of Nfe2l1 loss (Fig. 5A,C) in comparison to its impact on GC (Fig. 5B,C). Loss of Nfe2l1 in GC showed higher immune cell and inflammation markers (Fig. 5B). Investigating the differential expression pattern of the two muscle tissues, we found several genes to be oppositely regulated between soleus and GC such as *Cib2* or *Perp*, (Fig. 5D). Strikingly, GC of the mKO mice clusters closer to the WT of soleus than to control GC itself (Fig.5E), underlining the phenotypic switch of the GC tissue, being more similar to soleus in mKO animals (Fig. 2D-G). GO analysis (Fig. 5F) confirmed the imperative role of Nfe2l1 in energy metabolism and the UPS in GC muscle. Additionally, it pointed towards an impact on respiration, ATP metabolic processes, and muscle cell differentiation. Coherent with these data the metabolomics performed on GC showed tight

clustering of the two genotypes (Fig. 5G) and a strong difference in metabolites related to glucose metabolism and Warburg effect (Fig. 5H,I). In conclusion, this set of data showed a profound phenotypic change of GC tissue upon loss of Nfe2l1, while the impact on soleus was rather mild.

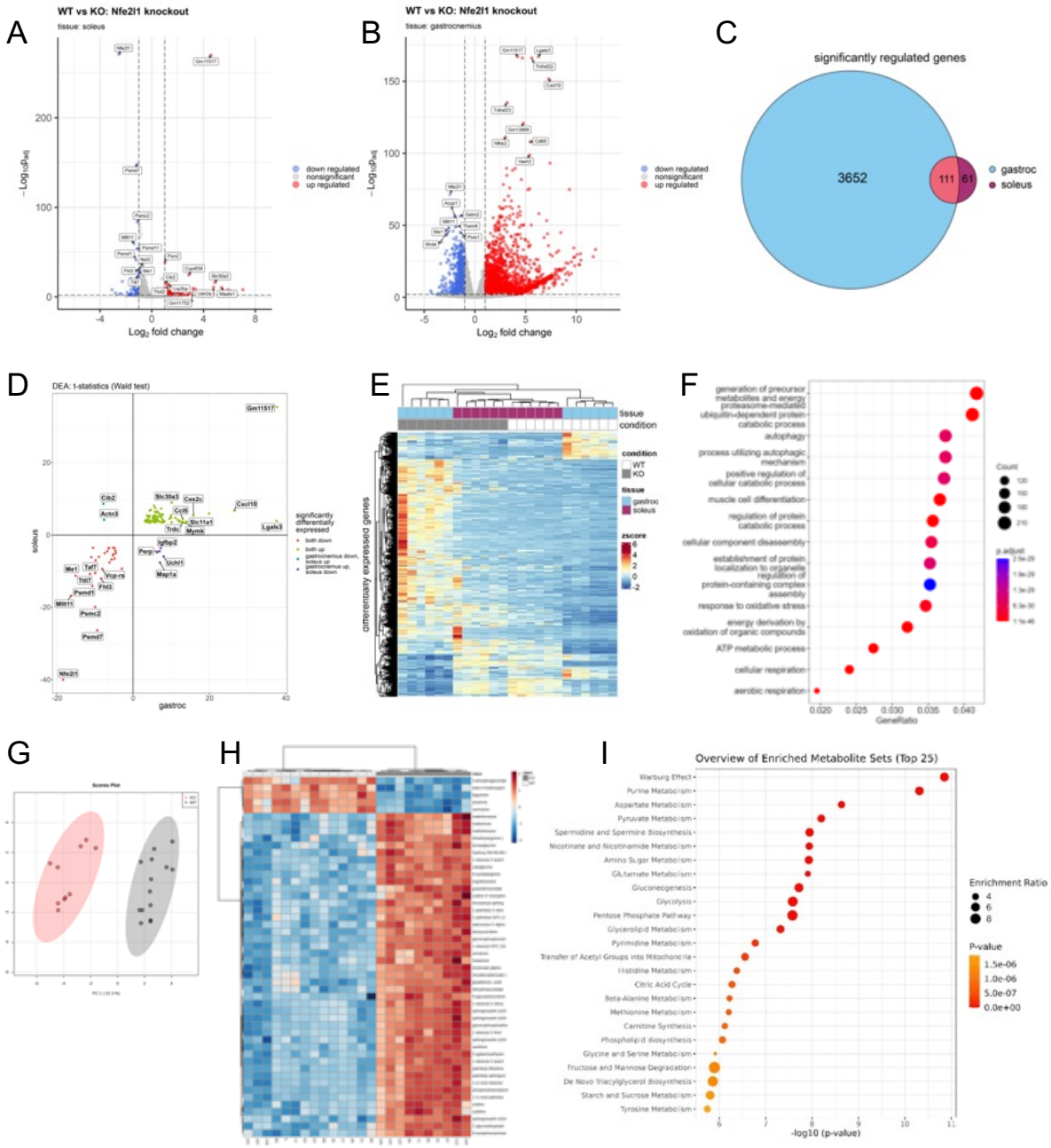

Figure 5: Multi-omics reveal differential metabolic impact of Nfe2l1 on muscle fibers.
(A-F) RNAseq analysis of gastrocnemius and soleus muscle (*n* = 6 mice per group): (A,B) Volcano plot of regulated genes of (A) soleus tissue and (B) GC tissue. (C) Euler diagram of significantly regulated genes in GC and soleus. (D) Scatter plot of significantly regulated genes in soleus compared to GC in *Nfe2l1* mKO mice. (E) Heatmap of differentially expressed genes in GC and soleus of WT controls and mKO mice. (F) GO enrichment analysis of top regulated pathways in GC tissue. (G-I) Metabolomics of GC tissue of *Nfe2l1* mKO mice and WT controls (*n* = 10 - 14 mice per group). (G) PCA analysis of metabolic phenotypes in WT and mKO mice. (H) Heatmap of metabolome profile of the different genotypes. (I) Top enriched metabolite sets in GC tissue. RNAseq data are mean ±SEM, p<0.01 by *t*-test (A-F) and metabolomics data are mean ±SEM, p<0.05 by 2-way-ANOVA (G-I).

Systemic energy metabolism is regulated by myocyte Nfe2l1 in vivo.

Next, we asked if the cellular phenotype of *Nfe2l1* mKO mice translated into altered whole-body energy metabolism. Using indirect calorimetry, we neither found differences in respiratory exchange ratio (RER) (Fig. 6A) nor in oxygen consumption per mouse on a regular chow diet (Fig. 6B,C). However, considering the lower body weight and lean mass of mKO mice as co-variates, we performed linear regression modeling of energy expenditure against body weight and found that energy expenditure was higher in the *Nfe2l1* mKO mice compared to WT controls (Fig. 6D). Interestingly, mKO displayed higher food intake (Fig. 6E), but no evident differences in physical activity (Fig. 6F). This indicates that the animals ate more to fuel their elevated energy expenditure.

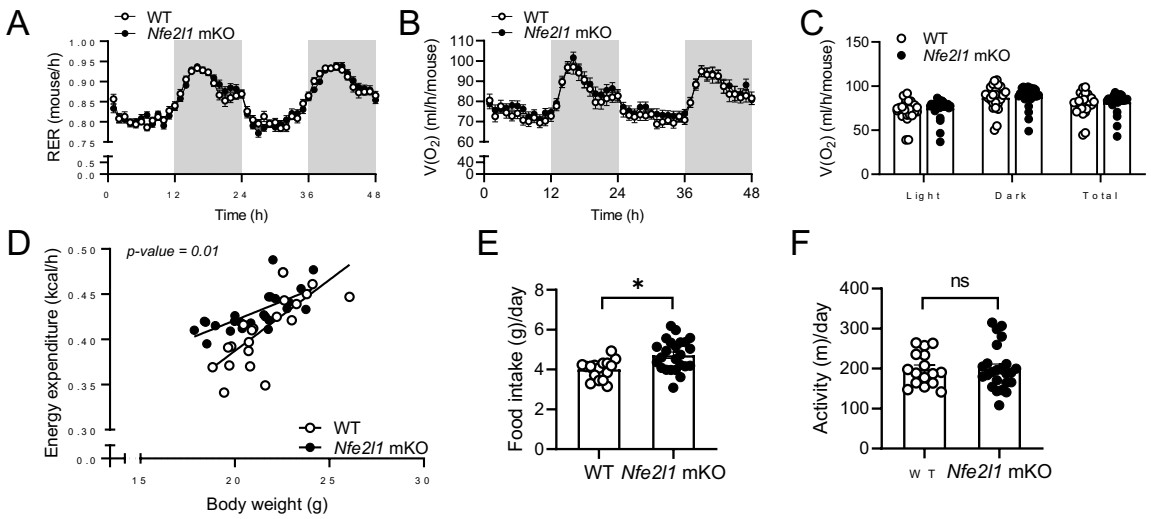

Figure 6: Myocyte Nfe2l1 is a critical regulator of energy expenditure and food intake.
(A-F) Measurements of WT and *Nfe2l1* mKO mice on chow diet at 6 weeks of age. (A) Respiratory exchange ratio, (B) Traces and (C) Quantification of oxygen consumption ((A-C): *n* = 26-28 mice per group). (D) Energy expenditure determined by indirect calorimetry over body weight (*n* = 22-24 mice per group). (E) Food intake. (F) Physical activity ((E,F): *n* = 16-24 mice per group). Data are mean ±SEM, p<0.05 by linear modeling (D) or *t*-test (C,E,F).

Loss of myocyte Nfe2l1 protects mice from weight gain and metabolic imbalance.

These findings raised the question how *Nfe2l1* mKO mice would respond to HFD feeding in terms of weight gain and metabolic health. We fed mKO and control mice HFD over 16 weeks and monitored body weight gain. HFD feeding led to the body weight difference becoming more pronounced, as the mKO mice were resistant to weight gain whilst the controls became obese (Fig. 7A,B, Extended Data Fig. 2), despite food intake being higher in mKO mice compared to WT controls (Extended Data Fig. 2). Linear regression modeling of indirect calorimetry data of energy expenditure and body weight revealed higher energy expenditure of the mKO on HFD compared to HFD-fed WT controls (Fig. 7C). Furthermore, glucose and insulin tolerance assessed by intraperitoneal glucose tolerance tests (GTT) (Fig. 7D) and insulin tolerance tests (ITT) (Fig. 7E) showed a significant difference between WT and mKO animals on HFD: The HFD-fed mKO mice displayed lower glucose and insulin tolerance compared to chow-fed mKO mice but showed a better response compared to WT animals fed with HFD. WT and mKO on chow diet showed similar GTT and ITT responses. In addition, we measured fasting plasma insulin levels and adiponectin concentrations: While there was no difference in chow-fed animals, mKO had lower insulin levels compared to WT controls when

fed a HFD (Fig. 7F). Adiponectin plasma levels were lower in mKO mice on HFD compared to WT controls and interestingly also lower than *Nfe2l1* mKO on chow diet (Fig. 7G). In line with weight gain resistance of mKO animals, leptin was higher in HFD-fed WT compared to HFD-fed mKO mice (Fig. 7H). Of note, leptin levels in chow-fed animals were indifferent. Cholesterol levels increased in both genotypes on HFD yet remained significantly lower in mKO mice in comparison to WT controls (Fig. 7I). Lastly, triglyceride levels were only significantly increased in mKO mice on HFD (Fig. 7J). Altogether, the *Nfe2l1* mKO animals showed a high-energy expenditure phenotype, which protected the animals from DIO and HFD-induced detrimental metabolic effects. Our results show a strong impact of insufficient proteasomal activity caused by loss of myocyte Nfe2l1 on muscle mitochondrial bioenergetics and energy metabolism.

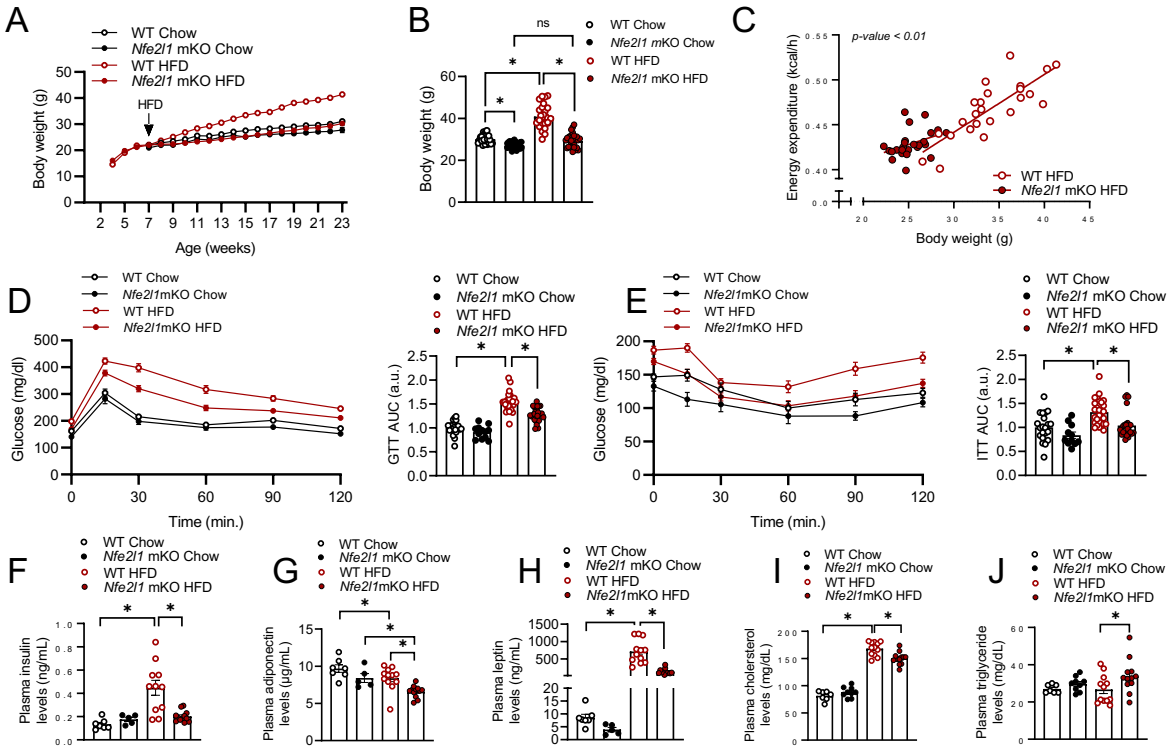

Figure 7: Absence of myocyte *Nfe2l1* improves energy metabolism and metabolic health.
(A) Body weight development of WT controls and *Nfe2l1* mKO mice on chow or HFD over 16 weeks of diet and (B) Body weight after 16 weeks of diet. (C) Energy expenditure after 8 weeks of HFD feeding over body weight. (A-C: (n = 24-27 mice per group)). (D) Traces and quantification (area under curve (AUC)) of intraperitoneal glucose tolerance test (i.p. GTT). (E) Traces and quantification (AUC) of intraperitoneal insulin tolerance test (i.p. ITT). (D,E: (n = 11-27 mice per group)). (F-J) Plasma analysis of WT controls and *Nfe2l1* mKO mice on Chow or HFD after 16 weeks of diet: (F) Insulin levels, (G) Adiponectin levels, (H) Leptin levels, (I) Cholesterol levels and (J) Triglycerides levels. ((F-J): n = 5-12 mice per group.) The data are mean ±SEM, $p<0.05$ by 2-way ANOVA (B,D-J) or linear modeling (C).

Discussion

Proteostasis is a critical component of metabolic adaptation. Adapting the proteome to metabolic demand, especially in tissues experiencing large fluctuations in metabolic rate such as skeletal muscle is paramount to maintaining energetic homeostasis and cellular integrity. Here, we show that proteasomal activity and management of ubiquitin levels in muscle is a regulated and critical process in obesity, as proteasome levels and function are increased in obesity. Interestingly, at the same time, total ubiquitin levels are largely unchanged, which suggests a dynamic recalibration of the rates of protein synthesis and degradation, including the processes necessary for ubiquitylation and its targets. By far, the most abundant modification is K48, which indicates that the proteasomal degradation pathway shapes the muscle ubiquitome under these conditions, which was linked to Nfe2l1 activation.

Generally, proteasomal degradation is a mechanism to defuse and/or recycle damaged or obsolete proteins. Obesity is associated with insulin resistance, aberrant lipid metabolism, and mitochondrial dysfunction, all of which lead to increased reactive oxygen species and protein damage[25]. Ubiquitylation as a means for marking proteins for degradation will create higher proteasomal demand[26]. However, for proteostatic sustainability, proteasomal content must be matched to the rates of ubiquitylation[26]. In other words, when proteasomal activity is insufficient or compromised, new proteasomes must be produced. This adaptive component of the UPS is mediated by Nfe2l1, and we show that Nfe2l1 is critical for myocyte proteasome function. However, loss of Nfe2l1 did not completely abolish proteasomal activity, which indicates that the baseline of proteasome subunit gene expression is likely mediated by a different, less adaptive mechanism, which could be mediated by e.g., FoxO1[27]. Nfe2l1 is also linked to mTORC1 signaling, as sustained genetic activation of mTORC1 promotes Nfe2l1 activation, proteasomal activity, and muscle atrophy[28]. However, this study also demonstrated juxtaposed roles of the UPS in atrophy and proteome integrity, which is in line with our findings that loss of Nfe2l1 creates a lean phenotype. We also observed distinct changes in GC vs soleus muscle, with GC being much more affected by Nfe2l1 loss than soleus, pointing to fiber type-specific demands for proteasome function and/or a potentially altered regenerative capacity of these fibers.

Furthermore, we found that some components of proteasome activity are higher in cells or tissues lacking Nfe2l1, indicating a potential compensatory posttranslational modification of proteasome function. However, overall proteasomal activity was lower and ubiquitin levels higher, indicating the predominant role of Nfe2l1 determining rates of UPS in myocytes. Next to changes in total amount and activity, we also found that proteasome subunits accumulated in a hyperubiquitylated state (Extended Data Fig. 1A), but the relevance of this observation will need further investigation. Likely, somewhat paradoxically, this indicates that proteasome subunits themselves are regulated by proteasomal degradation and in the absence of proper proteasomal activity, these subunits might further exert dominant negative effects on proteasome assembly and/or activity. It will be interesting to understand the composition of proteasomes under these conditions, as this might reveal new biochemical levers of managing UPS activity. The accumulation of ubiquitylated proteins induces cellular stress and this is evident in our study. In addition to cytosolic degradation, proteasomal protein degradation also takes place at the ERAD or in the nucleus. Clearly, disturbances in UPS and ERAD cause ER stress and inflammation[10], which we also observe in our model. As polyubiquitin chains linked by Lys48 are the main driver for proteasomal degradation and Nfe2l1 loss impairs proteasome activity, a subsequent accumulation of K48 was anticipated. Nevertheless, other linkages were also significantly upregulated and suggest a greater impact of the loss of Nfe2l1 than solely on

the UPS. It will be relevant to investigate these sites and proteins in more detail to potentially discover new regulators of muscle biology in obesity.

In terms of generalized muscle function and health, there are parallels between impaired autophagy and diminished proteasome function, UPS, and ERAD. When autophagy is suppressed, such as in Pompe disease, this is associated with ubiquitylated protein inclusion bodies and markers of muscle damage[29]. In general, skeletal muscle weakness is associated with the accumulation of high molecular weight proteins and ubiquitylated protein inclusions, for example in sporadic inclusion body myositis and hereditary inclusion body myopathies[30], including those caused by mutations in valosin-containing protein VCP, also kown as p97, which interestingly is a critical component of ERAD and Nfe2l1 translocation across the ER membrane[31]. There seems to be profound crosstalk between proteostatic mechanisms in muscle, as we found in the proteome of Nfe2l1 mKO muscle that autophagy pathways are markedly upregulated, including p62 and LC3B levels (Extended Data Fig. 1B-C). Anyhow, the accumulation of ubiquitylated proteins is hallmark of muscle dysfunction and vice versa is causally linked to muscle damage when autophagy or UPS are compromised. However, markers of muscle atrophy were not increased upon loss of Nfe2l1 (Extended Data Fig. 1D), indicating that the phenotype of mKO should not be classified as atrophy, but rather a muscle lean, remodeling phenotype.

A puzzling observation that requires further discussion are the mitochondrial phenotype and altered energy metabolism of Nfe2l1 mKO mice. On the one hand, there is aberrant mitochondrial function in isolated fibers and mitochondria of mKO mice compared to WT controls. In addition, there is a fiber type shift in gastrocnemius, but not soleus, to a more oxidative phenotype. Regardless, on a regular diet, there is no baseline difference in whole-body RER, but increased energy expenditure and food intake. The interpretation is that this is congruent with an energy wasting phenotype based on energy tradeoffs between mitochondrial and glycolytic metabolism. Understanding these tradeoffs between nutrient fluxes and metabolic efficiency will require tracer studies to pinpoint the exact underlying changes and will further enhance our understanding of metabolic adaption of skeletal muscle. Uncoupling of mitochondria and loss of mitochondrial membrane potential in myocytes are associated with the induction of FGF21[32], a myokine that is implicated in regulating energy metabolism. We find that FGF21 and GDF15 expression were higher in muscle of mKO mice compared to WT controls, and for GDF15 also plasma levels were elevated (Extended Data Fig. 2A-D), which could indicate an adaptive response to proteotoxic stress with potential endocrine impact on systemic energy metabolism. This is particularly interesting compared to other Nfe2l1-associated outcomes in mouse models of metabolic fatty liver disease[33] or thermogenesis[10], in which loss of Nfe21l and subsequent proteasomal impairment are clearly and exclusively detrimental. In contrast, here we show that loss of Nfe2l1 in myocytes is well tolerated and results in a favorable metabolic profile. This is in line with the notion that skeletal muscle responds to stress in a hormetic fashion such as certain levels of reactive oxygen species in exercise are required for its beneficial adaptation[25,34].

In conclusion, our study demonstrates the rewiring of muscle UPS in obesity and its regulation by Nfe2l1. We highlight the adaptive component of proteasome function in muscle proteostasis, which is required for proper turnover of ubiquitylated proteins. Understanding the regulation of Nfe2l1 might generate a therapeutic handle to preserve muscle mass and health in obesity and beyond.

2 Materials and methods

2.1 Mice husbandry, tissue collection, and plasma analysis

All animal experiments were performed according to procedures approved by the animal welfare committees of the government of Upper Bavaria, Germany (ROB-55.2-2532.Vet_02-20-32) and performed in compliance with German Animal Welfare Laws. Animals for dietary induced obesity (DIO) experiments were C57BL/6JRj with 16 weeks of HFD and age-matched chow fed controls purchased from Janvier Labs. The Nfe2l1 floxed mice described previously.[10] were crossed with B6.Cg-Tg(ACTA1-cre)79Jme/J (The Jackson Laboratory) stock no. (006149) to create Nfe2l1 myocyte-specific knockout (mKO) mice and WT control littermates carrying floxed Nfe2l1 alleles yet being Cre negative (Cre^-). The Nfe2l1 mKO mice were bred in standard conditions (License: ROB-55.2-2532.Vet_02-30-32) and housed in individually ventilated cages (IVCs) at room temperature (22 °C), with a 12-h light–dark cycle, and fed chow-diet or high-fat diet (HFD) with 60 kJ% lard (Sniff, D12492) and water ad libitum. Indirect calorimetry was measured in a PromethionCore by Sable Systems. Body composition was measured by EchoMRI™. Mice were anesthetized with a xylazine/ketamine (30/150 mg/kg) (WDT) prior to blood sampling and perfusion with PBS (Thermo Fisher Scientific) with heparin (50 U/mL). Collected tissues were snap-frozen in liquid nitrogen and stored at -80 °C. Plasma Leptin (R&D Systems), Adiponectin (R&D Systems) and Insulin (Crystal Chem) were analyzed via ELISA kits according to the manufacturer's instructions. Plasma cholesterol and triacylglycerol levels were measured using a Beckman Coulter AU480 Chemistry Analyzer (Beckman Coulter, Brea, CA, USA). Glucose and insulin tolerance tests were conducted after 6 h of fasting by intraperitoneal (*i.p.*) administration of 1 mg/g glucose or 0.75 U/kg insulin in 0.2% wt/vol BSA in PBS. Forelimb grip strength was assessed in triplicates via the Bioseb grip strength test instrument (GS3).

2.2 Cell culture, treatments, and reverse transfection

For cellular experiments, we used immortalized C2C12 mouse myoblasts (Sigma-Aldrich, 91031101). All cells were kept at 37 °C, 5% CO_2 in DMEM Glutamax (Thermo) supplemented with 10% FBS (Sigma) and 1% Penicillin/Streptomycin (PenStrep (Sigma)). They were continuously kept between 30-80% confluency and split three times per week. Cells were used until their passage number exceeded 40. For differentiation, C2C12 cells were grown to 95% confluency followed by differentiation with DMEM Glutamax (supplemented with 2% horse serum (Sigma) and 1% PenStrep). The medium was replaced every day for 6 days. Differentiated cells were treated with DMSO (Sigma) or 100 nM bortezomib (SelleckChem) before harvest. For *in vitro* gene silencing, SMARTpool small interfering RNA (siRNA, Dharmacon) in Lipofectamine RNAiMAX transfection reagent (Thermo), was used according to manufacturer's instructions. Reverse transfection was performed on day two of differentiation using 30 nM siRNA. New differentiation medium was added 24 hours after transfection and cells were treated 48 h after transfection and harvested subsequently.

2.3 Gene expression analysis

NucleoSpin RNA kit (Macherey Nagel) was used according to the manufacturer's instructions, for RNA extraction. RNA concentrations were measured with a NanoDrop spectrophotometer (Implen). For complementary DNA (cDNA) preparation 500 ng RNA were added to 2 µl Maxima H Master Mix (Thermo) and the total volume adjusted 10 µL with H_2O. The cDNA solution was

diluted 1:40 in H_2O. Relative gene expression was measured with qPCR. Per reaction, 5 µL PowerUp™ SYBR Green Master Mix (Thermo), 4 µL cDNA, and 1 µL of 5 µM primer stock (Supplementary Table 1) were added. A Quant-Studio 5 RealTime PCR system (Thermo) 2 min 50 °C, 10 min 95 °C, 40 cycles of 15 sec 95 °C, 1 min 60 °C) was used for measurement of Cycle thresholds (Cts) of genes of interest. Data was normalized to *TATA-box binding protein (Tbp)* levels by the ΔΔCt-method. Relative gene expression is displayed as fold change to the appropriate experimental control groups. RNA sequencing (RNAseq) was performed by Novogene (UK). For library sequencing Illumina NovaSeq platforms were used, applying a paired-end 150 bp sequencing strategy (short-reads).

2.4 Protein isolation/analysis and citrate synthase activity

Protein extraction and immunoblotting were performed as previously described[35]. Briefly, cells or tissues were lysed in RIPA buffer (50 mM Tris pH 8 (Merck),150 mM NaCl (Merck), 5 mM EDTA (Merck), 1% IGEPAL® CA-630 (Sigma), 0.5% sodium deoxycholate (Sigma), 0.1% SDS (Roth)) containing cOmplete mini protease inhibitors (Sigma) and PhosSTOP™ (Roche Diagnostics) using a TissueLyser II (3 min, 30 Hz; Qiagen). Lysates were centrifuged for 15 minutes (21,000 *g*, 4 °C) and supernatant was collected. Protein concentrations were determined using the Pierce BCA Protein Assay (Thermo) according to the manufacturer's instructions. 15-35 µg protein per sample were denatured with 5% (vol/vol) 2-mercaptoethanol (Sigma) in LDS sample buffer (Thermo) for 5 minutes at 95 °C before they were loaded in Bolt™ 4–12% Bis-Tris (Thermo) or NuPAGE™ 12% (Thermo) gels. After separation, proteins were transferred onto a 0.2 µm PVDF membrane (Bio-Rad) using the Trans-Blot® Turbo™ system (Bio-Rad) at 25 V, 1.3 A for 7 min. For determination of protein concentration, the membrane was stained in Ponceau S (Sigma). Blocking occurred in Roti-Block (Roth) at room temperature for 1 h. Primary antibodies (Supplementary Table 2) were incubated overnight at 4 °C. Blots were washed 3 x for 7 min with TBS-T (200 mM Tris (Merck), 1.36 mM NaCl (Merck), 0.1% Tween 20 (Sigma)) and secondary antibodies (Supplementary Table 2) applied for 1 h at room temperature. The membranes were washed in TBS-T and developed using SuperSignal West Pico PLUS Chemiluminescent Substrate (Thermo) in a ChemiDoc imager (Bio-Rad). We normalized the protein bands to beta-tubulin with Image Lab software (Bio-Rad). For citrate synthase activity, 15-30 µg protein was added to the reaction buffer (20 mM Tris-HCl, pH 8.0 (Merck), 0.42 mM acetyl-coenzyme A (Sigma), 0.1 mM DTNB (Sigma)) and incubated for 5 min at 37 °C. Subsequently, 0.5 mM oxaloacetate was added and emission measured at 412 nm over a course of 5 min.

2.5 Proteasome activity

Cells were lysed in lysis buffer (40 mM TRIS, pH 7.2 (Merck), 50 nM NaCl (Merck), 5 mM $MgCl_2$ (hexahydrate) (Merck), 10% (vol/vol) glycerol (Sigma), 2 mM ATP (Sigma), 2 mM β-mercaptoethanol (Sigma). Proteasome Activity Fluorometric Assay II kit (UBPBio, J41110) was used according to manufacturer's instructions for assessment of activity. Fluorescence was measured in the Plate reader (Tecan). This assay allowed for chymotrypsin-like, trypsin-like, and caspase-like activity measurement. The results were normalized to protein content using Bio-Rad Protein Assay Kit II (Bio-Rad) according to manufacturer's instructions.

2.6 Native PAGE

The protocol for in-gel proteasome activity assay and following immunoblotting was previously described in detail[36]. Briefly, tissues were lysed in Lysis buffer (50 mM Tris-HCl pH 7.5, 5 mM $MgCl_2$, 2 mM DTT, 10% glycerol (vol/vol), 2 mM ATP, 0.05% Digitonin (v/v)), with a phosphatase inhibitor (PhosStop™, Roche). The suspensions were kept on ice for 20 min and subsequently centrifuged twice. Protein concentration was determined with Bio-Rad Protein Assay Kit II and 15 µg sample protein was loaded on a NuPAGE 3-8% Tris-Acetate gel (Thermo). The gel was run for 4 h at a constant voltage of 150 V. Next, the gel was incubated in an activity buffer (50 mM Tris, 1 mM DTT, 1 mM $MgCl_2$) with 0.05 mM chymotrypsin-like substrate Suc-Leu-Leu-Val-Tyr-AMC (Bachem) at 37 °C for 30 min. The fluorescent signal was measured via a ChemiDoc MP (Bio-Rad).

2.7 Histology and EM

For Hematoxylin and eosin (H&E) staining tissues were fixed in 4% formalin (Sigma) and dehydrated overnight (70% EtOH, 96% EtOH, 100% EtOH, Xylene (Sigma)) in an ASP200S (Leica) and consequently embedded in paraffin (Roth). Sections of 4-6 µm were produced using a microtome (Leica). Deparaffination and rehydration was performed using standard procedure by incubating in Xylene (2 x 5 min), 100% EtOH (2 x 10 dips), 96% EtOH (5 dips), 70% EtOH (3 dips), ddH_2O (10 dips). Staining occurred by incubation in hematoxylin, H_2O, eosin (5 min each) and subsequent dehydration. Slides were mounted with Histokitt II (Roth) and images were taken with DMi8 (Leica). For SDH staining cryosections were produced with a Cryotome CM3050S (Leica) at 4-6 µm and stained with nitroblue tetrazolium (1:1000 w/v (Thermo)) diluted in SDH stock solution (0.2 M sodium succinate, 0.2 M PBS (Sigma)). Sections were stained for 45 min at 37 °C, following rinsing with acetone and dehydrating with ethanol and xylene. For immunofluorescent staining sections were incubated with 4% mouse on mouse (MOM) IgG blocking solution (Vector) at room temperature, briefly washed with PBS and incubated for 1 hour at 37 °C with a mix of primary antibodies (DSHB (University of Iowa)) consisting of: BA-D5 (IgG2b, supernatant, 1:100 dilution) specific for MyHC-I, SC-71 (IgG1, supernatant, 1:100 dilution) specific for MyHC-2A and BF-F3 (IgM, purified antibody, 1:100 dilution) specific for MyHC-2B. Subsequently, washed 3 times with PBS and incubated with secondary antibodies (Jackson ImmunoResearch) for 45 min at 37 °C: goat anti-mouse IgG1, conjugated with DyLight488 fluorophore, goat anti-mouse IgG2b, conjugated with DyLight405 fluorophore, goat anti-mouse IgM, conjugated with DyLight549 fluorophore. Images were taken with ZOE™-fluorescent cell imager (Bio-Rad). For transmission electron microscopy animals were perfused with 0.9% w/v NaCl and subsequently with electron microscopy grade fixative buffer containing: 3% w/v glutaraldehyde, 3% w/v paraformaldehyde in phosphate buffer, pH 7.4 (Electron Microscopy Science). Tissues were stored in said buffer and processed as described previously[37]. In short, tissues were post-fixed with 2% osmium tetroxide and dehydrated through a graded ethanol series. The samples were subsequently cleared in propylene oxide, embedded in EPON 812 (Serva Electrophoresis GmbH) and finally cured for 20 h at 45 °C followed by additional 24 h at 60 °C. The resulting blocks were trimmed and sectioned into 60 nm thin slices with a Reichert-Jung Ultracut E ultramicrotome using a diamond knife (DiATOME Electron Microscopy Sciences). Silver-appearing sections were placed on a 150 µm mesh copper/rhodium grid (Plano GmbH). Samples were contrasted using alcoholic uranyl acetate and lead citrate. The sections were imaged using a Libra 120 transmission electron microscope (Carl Zeiss NTS GmbH) equipped with a SSCCD camera system (TRS, Olympus).

2.8 Protein digestion and purification

Protein digestion and DiGly peptide enrichment was performed as previously described[38,39]. Briefly, the gastrocnemius was lysed in SDC buffer (1% SDC in 100 mM Tris-HCl, pH 8.5) and boiled for 5 min at 95°C while shaking at 1000 rpm. Lysates were sonicated for 15 min (Bioruptor, Diagenode, cycles of 30 sec) and protein concentrations were determined using the Pierce BCA Protein Assay (Thermo). CAA and TCEP (final concentrations: 40 mM and 10 mM respectively) were added to 5 mg Protein. Samples were incubated for 10 min at 45 °C in the dark, shaking at 1000 rpm. Trypsin (1:50 w/w (Sigma)) and LysC (1:50 w/w (Wako)) were added and samples were digested overnight at 37°C while shaking at 1000 rpm. For proteome analysis, sample aliquots (~15 µg) were desalted in 3-layered SDB-RPS StageTips (Empore). Briefly, samples were diluted with 2% TFA in isopropanol (1:1) to a final volume of 200 µL. Thereafter, samples were loaded onto StageTips and sequentially washed with 200 µL of 1% TFA in isopropanol and 200 µL 0.2% TFA/2% ACN. Peptides were eluted with freshly prepared 60 µL of 1.25% ammonium hydroxide (NH_4OH)/80% ACN and dried using a SpeedVac centrifuge (Thermo). Dried peptides were resuspended in 6 µL 2% ACN/0.1% TFA. DiGly enrichment samples were diluted with 1% TFA in isopropanol (1:5). For peptide cleanup SDB-RPS cartridges (Strata™-X-C, 200 mg/6 ml, Phenomenex Inc.) were equilibrated with 8 bed volumes (BV) of 30% MeOH/1% TFA and washed with 8 BV of 0.2% TFA. Samples were loaded by gravity flow and sequentially washed twice with 8 BV 1% TFA in isopropanol and once with 8 BV 0.2% TFA/2% ACN. Peptides were eluted in two steps with 4 BV 1.25% NH_4OH/80% ACN each and diluted with ddH_2O to a final ACN concentration of 35% ACN. Subsequently, samples were dried via SpeedVac centrifuge overnight.

2.9 Diglycine (DiGly) peptide enrichment

For DiGly peptide enrichment the PTMScan® Ubiquitin Remnant Motif (K-ε-GG) (Cell Signaling) was used. The peptides were resuspended in immunoaffinity purification (IAP) buffer and sonicated (Bioruptor, Diagenode) for 15 min Protein concentration was determined by Pierce BCA Protein Assay (Thermo). Antibody coupled beads were cross-linked like previously described[39]. Briefly, one vial of antibody coupled beads was washed with cold cross-linking wash buffer (2000 *g*, 1 min). Subsequently the beads were incubated in 1 mL cross-linking buffer at room temperature for 30 min under gentle agitation. The reaction was stopped by washing twice with 1 mL cold quenching buffer (200 mM ethanolamine, pH 8.0) and incubating for 2 h in quenching buffer at room temperature under gentle agitation. Cross-linked beads were washed with cold IAP buffer and used directly for DiGly peptide enrichment. For DiGly enrichment 3 mg of peptide is used with 1/8 of a vial of cross-linked antibody beads. Peptides were added to the cross-linked beads and the volume was adjusted to 1 mL with IAP buffer and incubated for 2 h at 4 °C under gentle agitation. The beads were washed with cold IAP buffer and ddH_2O. The enriched peptides were eluted by adding 200 µL 0.2% TFA onto the beads and shaking 5 min at 1400 rpm. After centrifugation, the supernatant was transferred to SDB-RPS StageTips and the peptides washed, eluted, and dried as previously described for total proteome samples.

2.10 LC-MS/MS proteome and ubiquitome measurements

Liquid chromatography of total proteome and ubiquitome samples was performed on an EASY-nLC™ 1200 (Thermo) with a constant flow rate of 10 µL/min and a binary buffer system consisting of buffer A (0.1% formic acid) and buffer B (80% acetonitrile, 0.1% formic acid) at

60 °C. The column was in-house made, 50 cm long with 75 µm inner diameter and packed with C18 ReproSil (Dr. Maisch GmbH, 1.9 µm). The elution gradient for the ubiquitome started at 5% buffer B, increasing to 25% after 73 min, 50% after 105 min and 95% after 110 min. The gradient for the total proteome started at 5% buffer B and increased to 20% after 30 min, further increased at a rate of 1% per minute to 29%, following up to 45% after 45 min and to 95% after 50 min. The MS measurement was performed on a Thermo Exploris 480 with injection of 500 ng peptide. Fragmented ions were analyzed in Data Independent Acquisition (DIA) mode with 66 isolation windows of variable sizes. The scan range was 300 – 1650 *m/z* with a total scan time of 120 min, an Orbitrap resolution of 120,000 and a maximum injection time of 54 ms. MS2 scans were performed with a higher-energy collisional dissociation (HCD) of 30% at a resolution of 15,000 and a maximum injection time of 22 ms. The MS measurement of the total proteome was performed equivalently, yet including High-Field Asymmetric Waveform Ion Mobility (FAIMS) with a correction voltage of -50 V and a total scan time of 60 min. The injection time for the full scan was 45 s and the MS2 injection time was set to 22 s.

2.11 Proteome and Ubiquitome data analysis

DIA raw files were processed using Spectronaut (13.12.200217.43655) in directDIA mode. The FASTA files used for the peptide identification were: Uniprot Mus Musculus (10.03.2022) with 21989 entries, Uniprot Mus Musculus isoforms (10.03.2022) with 41771 entries and MaxQuant Contaminants for filtering (245 entries). Protein groups in the total proteomes were quantified through label free quantification, following the MaxLFQ algorithm. Analysis was performed via Perseus (version 1.6.2.3). The site tables for ubiquitome samples were created with the Perseus plugin “Peptide Collapse” (version 1.4.2)[40]. Values were log2-transformed and missing values were replaced by imputation from normal distribution with a width of 0.3 and downshift 1.8 sepereatly for each sample. Ubiquitome was normalized to total proteome. Comparison between conditions of proteome and ubiquitome was performed via Student’s *t*-test in R version 4.2.2 (p-value cutoff 0.1 and 0.2 for GO-analysis).

2.12 Non-targeted metabolomics, data processing, and analysis

Untargeted metabolomics of muscle and plasma was performed by the Metabolomics and Proteomics Core facility (MPC) at Helmholtz Munich (Neuherberg, Germany) as previously described.[41] Briefly, frozen muscle tissue was homogenized at 4 °C with 1.4 mm ceramic beads in water (5 µL/mg). To precipitate the protein and extract metabolites, 500 µL MeOH extraction solvent containing recovery standard compounds was added to each 100 µL of plasma or tissue homogenate. Supernatants were aliquoted and dried under nitrogen stream (TurboVap 96, Zymark) and stored at -80 °C until measurement. An ultra-high performance liquid chromatography-tandem mass spectrometry (UPLC-MS/MS) based analytical platform licensed by Metabolon (Durham, NC, USA) using Acquity UPLC (Waters) coupled to a Q Exactive mass spectrometer (Thermo) was used to measure the samples. Three separate UPLC-MS/MS injections were performed: two injections for analysis by UPLC-MS/MS positive ionizations, e.g., early and late eluting compounds, and one injection for analysis by UPLC-MS/MS negative ionization. The resulting MS/MS data were matched to Metabolon’s proprietary chemical library, which includes retention time, molecular weight (m/z), preferred adducts, and in-source fragments, as well as associated MS/MS spectra for all molecules in the library. Peak area counts were median-normalized. Metabolites with more than 50% missing values were excluded, and missing values were imputed by k-nearest-neighbor algorithm. Values were log10 transformed for univariate and statistical analyses.

2.13 Seahorse

Seahorse analysis was performed as described previously[42]. Briefly, gastrocnemii were removed and homogenized in 1 mL MIBI buffer (210 mM d-Mannitol (Sigma), 70 mM sucrose (Sigma), 5 mM HEPES (Roth), 1 mM EGTA (Roth), 0.5% (w/v) fatty acid-free BSA (Sigma), pH 7.2) via douncer (Carl Roth). The homogenate was centrifuged at 800 *g* for 10 min at 4 °C. The supernatant was centrifuged at 8000 *g* and the pellet washed twice more with MIBI buffer. The pellet was resuspended in MASI buffer (220 mM d-Mannitol (Sigma), 70 mM sucrose (Sigma), 10 mM KH_2PO_4 (Sigma), 5 mM $MgCl_2$ (Sigma), 2 mM HEPES (Roth), 1 mM EGTA (Roth), 0.2% (w/v) fatty acid-free BSA (Sigma), pH 7.2 at 37 °C) with 10 mM succinate (Sigma) and 2 mM pyruvate (Agilent) and the mitochondria concentration assessed by Pierce BCA Protein Assay (Thermo). The assay was performed on a Seahorse XF24-analyzer (Agilent) with 1 µg mitochondria, 16 mM ADP (Sigma), 1 µM Oligomycin (Sigma), 40 µM FCCP (Sigma), 25 µM Rotenone/AntimycinA (Sigma). Injections and mix/measurement cycle times for the assay are illustrated in Supplementary Table 3.

2.14 Oroboros

Mitochondrial respiration was measured in permeabilized skeletal muscle fibers using a high resolution respirometer (Oxygraph-2k, Oroboros Instruments) as previously described.[43] Briefly, all respiratory measurements were made in duplicates in a hyperoxygenated environment ([O_2], 450-200 nmol/mL) to avoid potential oxygen limitations of the respiration. Skeletal muscle fibers were permeabilized with saponin (50 µg/mL) for 30 min in BIOPS buffer followed by 2 x 10 min wash in respiration medium 5 (MiR05). Leak respiration was assessed after addition of 2 mM malate, 10 mM glutamate and 5 mM pyruvate. Next, NADH-linked respiration was measured by adding 5 mM ADP and 3 mM $MgCl_2$ followed by 10 mM Cytochrome C to evaluate outer membrane integrity. Oxidative phosphorylation capacity with simultaneous electron input of complex I and II was assessed with 10 mM succinate. Lastly, maximum respiration rate was determined by adding 1 mM FCCP. All respiratory rates were measured in MiR05 buffer (containing 110 mmol/L sucrose, 60 mmol/L potassium lactobionate, 20 mmol/L Hepes, 10 mmol/L KH_2PO_4, 1 g/L BSA, 0.5 mmol/L EGTA, 20 mmol/L taurine, 3 mmol/L $MgCl_2 \cdot 6H_2O$, pH 7.1) at 37 °C.

2.15 Statistics

Data were analyzed with ImageLab, Microsoft Excel, GraphPad Prism and R (4.2.2). Unless otherwise specified, data are shown as mean ± standard error of the mean (SEM), including individual measurements. Multiple Student's *t*-test was used for experiments when comparing two groups and one variable and two-ANOVA with Bonferroni post-hoc test was used for comparing two groups with two variables. If not declared otherwise, P-values lower than 0.05 were considered significant and are as such indicated in the graphs with an asterisk between groups, non-significant groups have no indication. For proteomic analyses p-value cutoff was 0.2 in GO analysis and 0.1 for further analyses. For the differential expression analysis of RNAseq, we used R package *limma*[44] to compute the p-values and adjust for hypothesis testing using FDR.

Acknowledgement

We thank Silvia Weidner, Thomas Pitsch, Daniela Hass, and Daniel Brandt for excellent technical assistance. We are grateful to Henrika Jodeleit and Carolin Muley for their help with animal experiments. We thank Anna Artati for assistance with metabolomics and Yvonne Jansen for supporting the histology experiments. Special thanks to Gökhan Hotamışlıgil for his continuous support during the project and to Sander Kersten, Patrick Schrauwen, and Wouter van Marken Lichtenbelt for their kind encouragement and guidance. We thank all Bartelt lab members for discussions and the enjoyable atmosphere. M.R. is funded by the European Research Council (ERC) under the European Union's Horizon 2020 research and innovation program (#949017), and Helmholtz Association - Initiative and Networking Fund. P.N. and M.P.M. thank the German Center for Diabetes Research (DZD) for funding. N.K. and D.T.H. are supported by Emmy-Noether DFG (KR5166/1-1). T.M. and Z.G.-H. were supported by funding from the Novo Nordisk Foundation Center for Basic Metabolic Research. A.B. was supported by the DFG Priority Program 2306 (BA 4925/2-1), the DFG CRC1123 on Atherosclerosis, the Deutsches Zentrum für Herz-Kreislauf-Forschung DZHK Junior Research Group Program (JRG), and the ERC Starting Grant PROTEOFIT. The graphical abstract was created using BioRender.com. We apologize to colleagues whose work we could not cite due to space limitations.

Competing interest

The authors declare no competing financial interests related to this work.

Author contributions

I.L. designed and performed experiments, analyzed data, and wrote the manuscript. D.H, N.W., E.G., I.T., and M.R. performed experiments and analyzed data. S.Kh., S.Ko. and S.H. analyzed data. D.H. and N.K. performed and analyzed proteomics data. D.T.E. and J.W. performed electron microscopy. S.L., T.M. and Z.G.-H. performed Oroboros measurements and analysis. K.D. performed and analyzed metabolomics data. A.B. made coffee, designed experiments, analyzed data, and wrote the manuscript. All authors read and commented on the manuscript.

References

1. Blüher, M. Obesity: global epidemiology and pathogenesis. *Nat. Rev. Endocrinol.* **15**, 288–298 (2019).
2. Hotamisligil, G. S. Inflammation, metaflammation and immunometabolic disorders. *Nature* **542**, 177–185 (2017).
3. Giroud, M. *et al.* HAND2 is a novel obesity-linked adipogenic transcription factor regulated by glucocorticoid signalling. *Diabetologia* **64**, 1850–1865 (2021).
4. Walter, P. & Ron, D. The Unfolded Protein Response: From Stress Pathway to Homeostatic Regulation. *Science (80-.).* **334**, 1081–1086 (2011).
5. Hotamisligil, G. S. Endoplasmic Reticulum Stress and the Inflammatory Basis of Metabolic Disease. *Cell* **140**, 900–917 (2010).
6. Hetz, C., Chevet, E. & Oakes, S. A. Proteostasis control by the unfolded protein response. *Nat. Cell Biol.* **17**, 829–838 (2015).

7. Pohl, C. & Dikic, I. Cellular quality control by the ubiquitin-proteasome system and autophagy. *Science (80-.).* **366**, 818–822 (2019).

8. Steffen, J., Seeger, M., Koch, A. & Krüger, E. Proteasomal Degradation Is Transcriptionally Controlled by TCF11 via an ERAD-Dependent Feedback Loop. *Mol. Cell* **40**, 147–158 (2010).

9. Sha, Z. & Goldberg, A. L. Multiple myeloma cells are exceptionally sensitive to heat shock, which overwhelms their proteostasis network and induces apoptosis. *Proc. Natl. Acad. Sci.* **117**, 21588–21597 (2020).

10. Bartelt, A. *et al.* Brown adipose tissue thermogenic adaptation requires Nrf1-mediated proteasomal activity. *Nat. Med.* **24**, 292–303 (2018).

11. Cui, M. *et al.* Nrf1 promotes heart regeneration and repair by regulating proteostasis and redox balance. *Nat. Commun.* **12**, 5270 (2021).

12. Rose, A. J. & Richter, E. A. Skeletal muscle glucose uptake during exercise: How is it regulated? *Physiology* 260–270 (2005) doi:10.1152/physiol.00012.2005.

13. Egan, B. & Zierath, J. R. Exercise Metabolism and the Molecular Regulation of Skeletal Muscle Adaptation. *Cell Metab.* **17**, 162–184 (2013).

14. Wu, J. *et al.* The Unfolded Protein Response Mediates Adaptation to Exercise in Skeletal Muscle through a PGC-1α/ATF6α Complex. *Cell Metab.* **13**, 160–169 (2011).

15. Kim, K. H. *et al.* Autophagy deficiency leads to protection from obesity and insulin resistance by inducing Fgf21 as a mitokine. *Nat. Med.* **19**, 83–92 (2013).

16. Milan, G. *et al.* Regulation of autophagy and the ubiquitin–proteasome system by the FoxO transcriptional network during muscle atrophy. *Nat. Commun.* **6**, 6670 (2015).

17. Masiero, E. *et al.* Autophagy Is Required to Maintain Muscle Mass. *Cell Metab.* **10**, 507–515 (2009).

18. Tezze, C. *et al.* Age-Associated Loss of OPA1 in Muscle Impacts Muscle Mass, Metabolic Homeostasis, Systemic Inflammation, and Epithelial Senescence. *Cell Metab.* **25**, 1374-1389.e6 (2017).

19. Muñoz, J. P. *et al.* Mfn2 modulates the UPR and mitochondrial function via repression of PERK. *EMBO J.* **32**, 2348–2361 (2013).

20. Deshmukh, A. Proteomics of Skeletal Muscle: Focus on Insulin Resistance and Exercise Biology. *Proteomes* **4**, 6 (2016).

21. Cervone, D. T., Moreno-Justicia, R., Quesada, J. P. & Deshmukh, A. S. Mass spectrometry-based proteomics approaches to interrogate skeletal muscle adaptations to exercise. *Scand. J. Med. Sci. Sport.* 1–17 (2023) doi:10.1111/sms.14334.

22. Goodman, C. A., Davey, J. R., Hagg, A., Parker, B. L. & Gregorevic, P. Dynamic Changes to the Skeletal Muscle Proteome and Ubiquitinome Induced by the E3 Ligase, ASB2β. *Mol. Cell. Proteomics* **20**, 100050 (2021).

23. Wefers, J. *et al.* Circadian misalignment induces fatty acid metabolism gene profiles and compromises insulin sensitivity in human skeletal muscle. *Proc. Natl. Acad. Sci.* **115**, 7789–7794 (2018).

24. Cogliati, S. *et al.* Mitochondrial Cristae Shape Determines Respiratory Chain Supercomplexes Assembly and Respiratory Efficiency. *Cell* **155**, 160–171 (2013).

25. Di Meo, S., Iossa, S. & Venditti, P. Skeletal muscle insulin resistance: role of mitochondria and other ROS sources. *J. Endocrinol.* **233**, R15–R42 (2017).

26. VerPlank, J. J. S., Lokireddy, S., Zhao, J. & Goldberg, A. L. 26S Proteasomes are rapidly activated by diverse hormones and physiological states that raise cAMP and cause Rpn6 phosphorylation. *Proc. Natl. Acad. Sci.* **116**, 4228–4237 (2019).

27. Kapetanou, M. *et al.* FoxO1 Is a Novel Regulator of 20S Proteasome Subunits Expression and Activity. *Front. Cell Dev. Biol.* **9**, (2021).

28. Kaiser, M. S. *et al.* Dual roles of mTORC1-dependent activation of the ubiquitin-proteasome system in muscle proteostasis. *Commun. Biol.* **5**, 1141 (2022).

29. Raben, N. *et al.* Suppression of autophagy in skeletal muscle uncovers the accumulation of ubiquitinated proteins and their potential role in muscle damage in Pompe disease. *Hum. Mol. Genet.* **17**, 3897–3908 (2008).

30. Watts, G. *et al.* Novel VCP mutations in inclusion body myopathy associated with Paget disease of bone and frontotemporal dementia. *Clin. Genet.* **72**, 420–426 (2007).

31. Radhakrishnan, S. K., den Besten, W. & Deshaies, R. J. p97-dependent retrotranslocation and proteolytic processing govern formation of active Nrf1 upon proteasome inhibition. *Elife* **3**, (2014).

32. Keipert, S. *et al.* Skeletal muscle mitochondrial uncoupling drives endocrine cross-talk through the induction of FGF21 as a myokine. *Am. J. Physiol. Metab.* **306**, E469–E482 (2014).

33. Widenmaier, S. B. *et al.* NRF1 Is an ER Membrane Sensor that Is Central to Cholesterol Homeostasis. *Cell* **171**, 1094-1109.e15 (2017).

34. Merry, T. L., MacRae, C., Pham, T., Hedges, C. P. & Ristow, M. Deficiency in the ROS-sensing Nuclear Factor Erythroid 2-like 2 (Nrf2) causes altered glucose and lipid homeostasis following exercise training. *Am. J. Physiol. Physiol.* ajpcell.00426.2019 (2019) doi:10.1152/ajpcell.00426.2019.

35. Muley, C., Kotschi, S. & Bartelt, A. Role of Ubiquilins for Brown Adipocyte Proteostasis and Thermogenesis. *Front. Endocrinol. (Lausanne).* **12**, (2021).

36. Yazgili, A. S. *et al.* In-gel proteasome assay to determine the activity, amount, and composition of proteasome complexes from mammalian cells or tissues. *STAR Protoc.* **2**, 100526 (2021).

37. Egu, D. T., Walter, E., Spindler, V. & Waschke, J. Inhibition of p38MAPK signalling prevents epidermal blistering and alterations of desmosome structure induced by pemphigus autoantibodies in human epidermis. *Br. J. Dermatol.* **177**, 1612–1618 (2017).

38. Hansen, F. M. *et al.* Data-independent acquisition method for ubiquitinome analysis reveals regulation of circadian biology. *Nat. Commun.* **12**, (2021).

39. Udeshi, N. D., Mertins, P., Svinkina, T. & Carr, S. A. Large-scale identification of ubiquitination sites by mass spectrometry. *Nat. Protoc.* **8**, 1950–1960 (2013).

40. Bekker-Jensen, D. B. *et al.* Rapid and site-specific deep phosphoproteome profiling by data-independent acquisition without the need for spectral libraries. *Nat. Commun.* **11**, 787 (2020).

41. Artati, A., Prehn, C., Lutter, D. & Dyar, K. A. Untargeted and Targeted Circadian Metabolomics Using Liquid Chromatography-Tandem Mass Spectrometry (LC-MS/MS) and Flow Injection-Electrospray Ionization-Tandem Mass Spectrometry (FIA-ESI-MS/MS). in 311–327 (2022). doi:10.1007/978-1-0716-2249-0_21.

42. Wettmarshausen, J. & Perocchi, F. Isolation of Functional Mitochondria from Cultured Cells and Mouse Tissues. in 15–32 (2017). doi:10.1007/978-1-4939-6824-4_2.

43. Pesta, D. & Gnaiger, E. High-Resolution Respirometry: OXPHOS Protocols for Human Cells and Permeabilized Fibers from Small Biopsies of Human Muscle. in 25–58 (2012). doi:10.1007/978-1-61779-382-0_3.

44. Ritchie, M. E. *et al.* limma powers differential expression analyses for RNA-sequencing and microarray studies. *Nucleic Acids Res.* **43**, e47–e47 (2015).

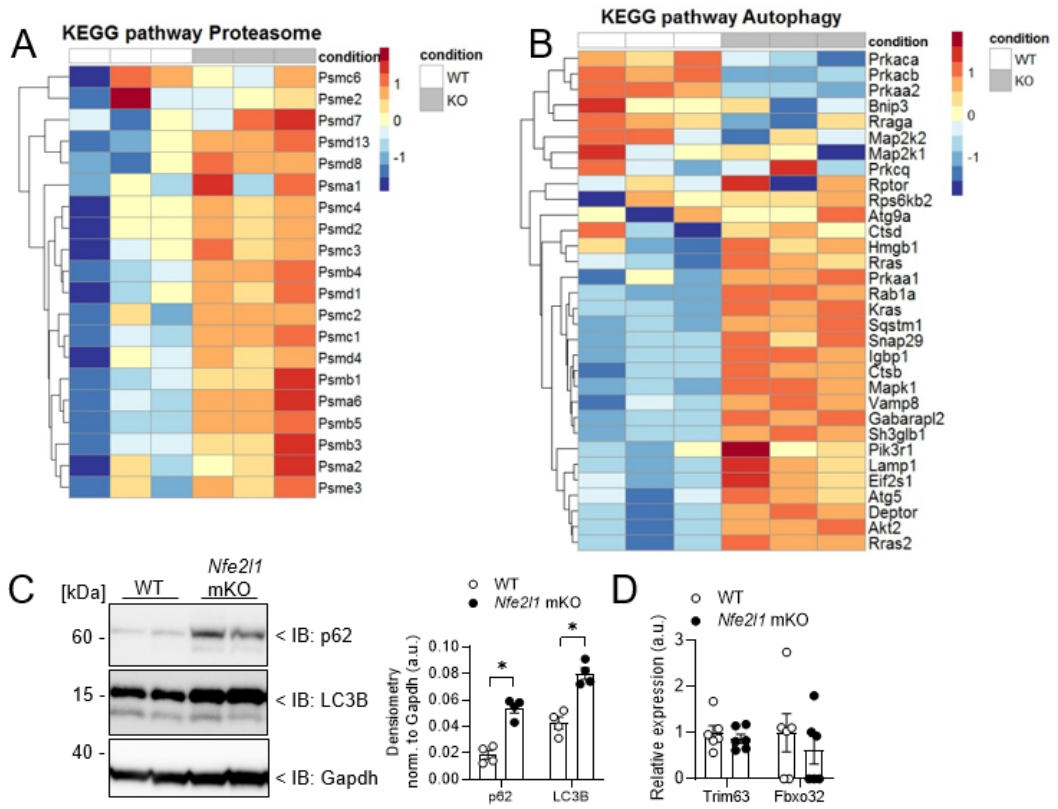

Extended Data Figure 1: Loss of Nfe2l1 impacts autophagy but not muscle atrophy markers. (A) KEGG analysis (03050) of proteasome from ubiquitome of WT and *Nfe2l1* mKO mice. (B) KEGG-pathway analysis (mmu04140) from total proteome of mKO and WT mice. (C) Immunoblot and quantification of p62, LC3B to Gapdh in GC of mKO and WT mice. (D) Relative expression levels of Trim63 and Fbxo32 in GC of control and *Nfe2l1* mKO animals.

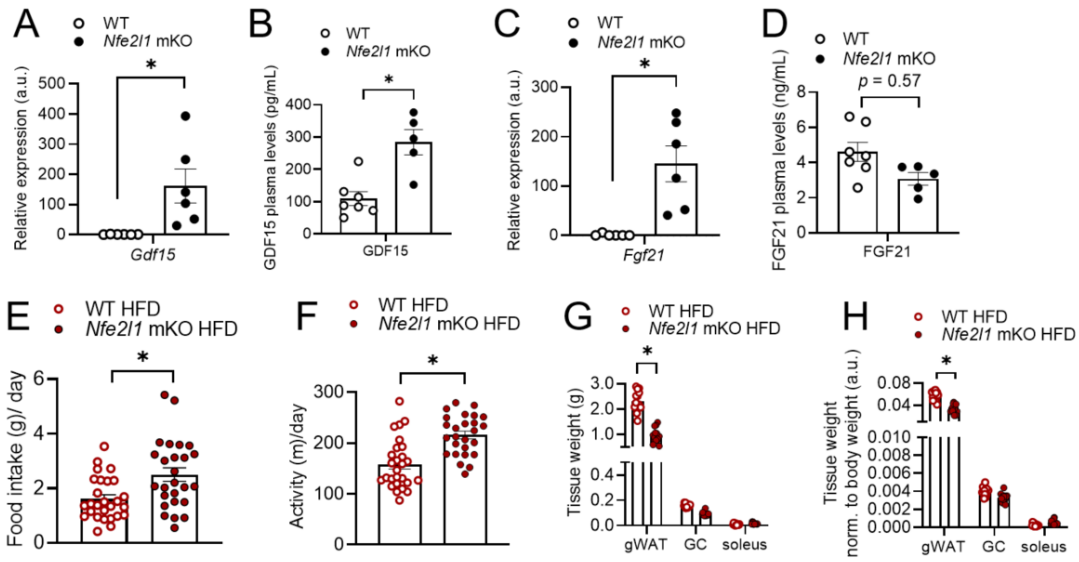

Extended Data Figure 2: Absence of Nfe2l1 leads to myokine secretion and increased food intake on HFD. (A) Relative *Gdf15* mRNA expression and (B) plasma levels of GDF15 in WT and mKO mice. (C) Relative *Fgf21* mRNA expression and (D) plasma levels of FGF21 in *Nfe2l1* mKO mice and WT controls. ((A-D) *n*= 5 -7 mice per group.) (E) Food intake and (F) activity of WT and mKO mice on HFD (*n* = 26 – 27 mice per group). (G) Tissue weight of gWAT, GC and soleus and (H) Tissue weight normalized to body weight of mKO and WTs on HFD (*n* = 14 – 15 mice per group).

Supplementary Table 1:

Gene	Forward Primer (5')	Reverse Primer (3')
Nfe2l1	GACAAGATCATCAACCTGCCTGTAG	GCTCACTTCCTCCGGTCCTTTG
Psma1	TGCGTGCGTTTTTGATTTTAGAC	CCCTCAGGGCAGGATTCATC
Psmb1	CGTTGAAGGCATAAGGCGAAAA	TTCCACTGCTGCTTACCGAG
Tbp	AGAACAATCCAGACTAGCAGCA	GGGAACTTCACATCACAGCTC

Supplementary Table 2:

Antibody	Company (Cat. No.)	Dilution
20S Proteasome α subunits	Abcam (ab22674)	1:1000
Akt	Cell signaling technologies (9272)	1:1000
eIF2α	Cell signaling technologies (9733)	1:1000
Gapdh	Cell signaling technologies (5174)	1:1000
LC3B	Cell signaling technologies (2775)	1:1000
Nfe2l1	Cell signaling technologies (D9K6P)	1:500
Total OXPHOS rodent	Abcam (ab110413)	1:1000
p62	Abcam (ab155686)	1:1000
p-Akt (Ser)	Cell signaling technologies (4051)	1:1000
p-eIF2α	Cell signaling technologies (3597)	1:1000
Ubiquitin (P4D1)	Cell signaling technologies (3936)	1:1000
β-tubulin	Cell signaling technologies (2146)	1:1000
Anti-rabbit IgG, HRP-linked	Cell signaling technologies (7074)	1:10000
Anti-mouse IgG, HRP-linked	Cell signaling technologies (7076)	1:10000

Supplementary Table 3:

Command	Time
Baseline	Wait: 00:10:00 Mix: 00:01:00 Wait: 00:03:00 Duration: 00:14:00
Measurement Baseline	Mix: 00:01:00 Wait: 00:00:00 Measure: 00:03:00 Cycles: 2 Duration: 00:08:00
ADP (Port A)	Mix: 00:01:00 Wait: 00:00:00 Measure: 00:04:00 Cycles: 1 Duration: 00:05:00
Oligo (Port B)	Mix: 00:01:00 Wait: 00:00:00 Measure: 00:03:00 Cycles: 1 Duration: 00:04:00
FCCP (Port C)	Mix: 00:01:00 Wait: 00:00:00 Measure: 00:03:00 Cycles: 1 Duration: 00:04:00
Rot/AA (Port D)	Mix: 00:01:00 Wait: 00:00:00 Measure: 00:03:00 Cycles: 2 Duration: 00:08:00